RSC Advances

ROYAL SOCIETY OF CHEMISTRY

www.rsc.org/advances

Journal Name

RSCPublishing

ARTICLE

A High Performance Supercapacitor Based on Ceria/Graphene Nanocomposite Synthesized by a Facile Sonochemical Method

Cite this: DOI: 10.1039/x0xx00000x

Received 00th January 2012,
Accepted 00th January 2012

DOI: 10.1039/x0xx00000x

www.rsc.org/

Amin Shiralizadeh Dezfuli,[a] Mohammad Reza Ganjali,[*ab] Hamid Reza Naderi [a] and Parviz Norouzi[ab],

In this work, we have developed a novel nanocomposite material of ceria (CeO_2)-reduced graphene oxide (RGO) by sonochemical route for the application as symmetric supercapacitors. CeO_2 nanoparticles have been anchored on RGO sheets in order to maximize the specific capacitances of these materials. Nanostructure studies and electrochemical performances of the CeO_2 nanoparticles on the RGO sheets were systematically investigated. The morphology and crystalline structure of nanocomposites were examined by field emission scanning electron microscopy (FE-SEM), Fourier transform infrared (FT-IR), and X-ray diffraction (XRD). Electrochemical properties of the nanocomposite electrodes were examined by cyclic voltammetry (CV), galvanostatic charge/discharge and electrochemical impedance spectroscopy (EIS) measurements. CeO_2-RGO nanocomposite electrodes exhibited excellent supercapacitive behavior with high specific capacitance of (211 F g^{-1} at 2 mV s^{-1} and 185 F g^{-1} at 2.0 A g^{-1}), high rate capability and well reversibility. Cycling stability of electrode was measured by continues cyclic voltammetry (CCV) technique. Upon 4000 cycles, the specific capacitance of the electrode increases and reaches a maximum value of 105.6 % of the initial value.

Introduction

Supercapacitors are promising electrical energy storage devices. They have higher energy density than conventional electrical double-layer capacitors while possessing higher power density, faster charging/discharging rate capability, and longer cycle-life than batteries. [1-3]

Supercapacitors are classified into two major types based on the charge-storage mechanisms: electrical double-layer capacitors (EDLCs) and pseudocapacitors. The former type employs carbon based materials as main electrode materials where the latter type employs electroactive materials including noble and transition metal oxides or conducting polymers as electrode materials.[4] Among carbon based materials, graphene has been proposed to be a promising candidate for supercapacitor applications due to its attractive properties such as chemical and thermal stability, excellent electrical conductivity, and high surface area. While pristine graphene cannot be produced in bulk quantities, [5] reduced graphene oxide (RGO), a chemically functionalized graphene, provides an appropriate pathway for producing large scale, inexpensive, and high-yield production of graphene based materials via solution process. [6]

Recently, decoration of RGO with various nanomaterials attracted huge interests as it allows one to gain a new class of hybrid materials with properties that are different from those of each individual component. [6-10] Currently, some nanoparticles such as metal oxides have been designed to be introduced into the interlayers of graphene sheets. This decoration prevents RGOs from restacking and thus maintains the high surface area

of graphene nanosheets, and makes both sides of the nanosheets accessible to the electrolyte. While the metal oxide nanoparticles such as RuO_2, SnO_2, Mn_3O_4 and MnO_2 function as spacers in metal oxide anchored graphene composites, [11] the resultant composites exhibit superior capacitance values and energy density than EDLCs as these nanoparticles can contribute pseudocapacitance generated by redox reactions. [1, 3, 11-13]

Nanoparticles of ceria (CeO_2) can be considered as one of the promising redox supercapacitor materials since CeO_2 is the most abundant and least expensive rare earth metal oxide with excellent redox characteristics. [6] Furthermore, its nanostructure with higher surface area has prominent effect on pseudocapacitance. [2] Recently, Li and co-workers utilized an in situ method to synthesize CeO_2-graphene nanocomposite, which showed a specific capacitance of 208 Fg^{-1} and a maximum power density of 18 kW kg^{-1} in supercapacitors. [2]
In the present study, we have developed synthesis procedure of CeO_2–RGO composites through a facile and efficient sonochemical method. In this method, sonication not only caused uniform dispersion of CeO_2 nanoparticles anchored on the surface of graphene oxide but also facilitated the self-assembly process. Then, we investigated the supercapacitive behavior of CeO_2–RGO composite electrodes by cyclic voltammetry (CV), electrochemical impedance spectroscopy (EIS) and galvanostatic charge/discharge measurements in a 0.5 M Na_2SO_4 electrolyte.

Experimental

Materials

Graphite flakes, cerium(III) nitrate hexahydrate ($Ce(NO_3)_3.6H_2O$), phosphoric acid (H_3PO_4), hydrazine hydrate (N_2H_4) and ammonium hydroxide (NH_4OH) were purchased from Sigma-Aldrich Co. Potassium permanganate ($KMnO_4$), sulfuric acid (H_2SO_4), hydrochloric acid (HCl), and hydrogen peroxide (H_2O_2) were all purchased from Merck Chemical Co. All reagents were used without any further modification.

Preparation of GO

Graphene oxide (GO) was prepared from natural graphite flake powder according to the Tour's method.[14] In specific, 3 g of graphite flake powder was added to 400 mL of a mixture of concentrated H_2SO_4/H_3PO_4 (9:1). While maintaining vigorous stirring, 18 g of $KMnO_4$ was slowly added to the suspension. After that, the mixture was stirred at 50 °C for 12 h. Then, the reaction was cooled to room temperature and poured onto 400 g of ice containing 5 mL of 30% H_2O_2 solution and the color became bright yellow. For purification, the reaction mixture was centrifuged and the remaining solid was washed 3 times with 5% HCl solution and then, repeatedly washed with distilled water until the pH of the dispersion became neutral. The as-prepared graphite oxide was vacuum-dried at room temperature. Finally, 150 mg of graphite oxide was dispersed in 300 mL of distilled water using an ultrasonic probe (UP400S Hielscher - Ultrasound Technology, Germany) for 3 h, leading to the formation of a light-brown suspension of GO.

Preparation of CeO_2–RGO nanocomposite

The CeO_2–RGO nanocomposite was prepared through a facile sonochemical method. This procedure involves three steps: At the first step, 0.35 mmol of $Ce(NO_3)_3.6H_2O$ was dissolved in 30 mL of distilled water. During the ultrasound irradiation (in an ultrasonic bath, FALC instruments ultrasonic), a 32% NH_4OH aqueous solution was added drop-wise to the above solution. This process was performed within 66 min. Secondly, 60 mL of GO (0.5 mg/ml) was added into the suspension under vigorous stirring, and sonicated for another 22 min. Subsequently, the mixture suspension was heated to 90 ◦C, 3 mL of N_2H_4 was added and the mixture suspension was refluxed for 1 h. The resulting precipitate was washed several times with ethanol and distilled water before drying at 60 ◦C for 24 h. Finally the obtained composite was designated as CeO_2–RGO, in which the theoretical mass ratio of CeO_2 to GO is 2:1. For comparison, pure CeO_2 and RGO samples were also prepared through the same procedure.

Characterizations

The crystalline phase compositions of the samples were characterized by X-ray diffraction (XRD) on a Philips PW-1730 X-ray diffractometer using Cu K_α radiation (λ = 1.5405Å). The morphology of the products were characterized by field-emission scanning electron microscopy (FE-SEM) on a Zeiss SIGMA VP with gold coating. Fourier transform infrared spectroscopy (FT-IR) spectra were recorded on a BRUKER EQUINOX 55 spectrophotometer. Raman spectra were obtained from Almega Thermo Nicolet Dispersive Raman Spectrometer applying 532 nm laser's light.

Electrochemical Measurements

The electrochemical measurement was carried on an Autolab PGSTAT30 with a three-electrode cell at room temperature in 0.5 M Na_2SO_4 solution as electrolyte. The electrolytes were degassed with nitrogen gas for at least 15 min before electrochemical measurements. The counter and the reference electrodes are a Pt foil and an Ag/AgCl (saturated KCl) electrode, respectively. The working electrodes were prepared by mixing active materials with 10 wt % acetylene black and 5 wt % polytetrafluoroethylene (PTFE). A small amount of ethanol was added dropwise into the above mixture to form a slurry by sonication. The slurry was pressed on a stainless steel current collector. Each working electrode contained about 1 mg of electroactive material and had a geometric surface area of about 1 cm^2. The as-prepared electrode was dried at room temperature for 4 h.
Cycling stability of electrode is measured by continues cyclic voltammetry (CCV) technique. The CCV data collection was achieved with the help of the following equipment; a setup of a computer, equipped with a data acquisition board (PCL-818HG, Advantech. Co.) and a custom made potentiostat described in our previous works.[15, 16] All data acquisition and

data processing programs were developed in a Delphi6® program environment.

Results and discussion

Synthesis of CeO_2-RGO nanocomposite

Generally, there are two different approaches to design and control synthesis of graphene-based nanocomposites. In the first approach, precursor salts adsorb on the surface of graphene or graphene oxide and nanoparticles grow directly (*in situ* growth) while in the second approach, as-synthesized nanoparticles anchor to the surface of graphene or graphene oxide (*self-assembly* approach).[10]

Herein, we have used a self-assembly approach to anchor CeO_2 nanoparticles on the RGO surfaces by utilizing an ultrasonic bath, a schematic diagram of the preparation process is illustrated in Scheme 1. Ultrasound creates the extremely high local temperature (>5000 K), pressure (>20 MPa) and heating and cooling rates ($>10^{10}$ Ks^{-1}) due to acoustic cavitation phenomena. [17-19] These conditions provide energy to generate CeO_2 nuclei, while the production and adsorption of bubbling gases on nuclei surface reduce the interfacial free energy between nuclei and solution, consequently prevent the growth of particles. Accordingly, the rapid nucleation followed by the slower grain growth leads to smaller particle sizes. While GO with a large amount of functional groups provides sites for anchoring of CeO_2 nanoparticles to reduce the total energy of the system through the self-assembly process, the collapse of the bubbles promotes the attachment of nanoparticles on the GO surface through high-speed liquid jets to the solid surface.

Characterization of nanocomposite

XRD. The XRD patterns of GO, RGO, CeO_2 and CeO_2–RGO are shown in Fig. 1. The diffraction peak at $2\theta = 12.2°$ in the pattern of GO is from the (001) reflection of graphite oxide corresponding to a d-spacing of 0.72 nm. This indicates that the flake-graphite was oxidized into graphite oxide. The absence of this characteristic diffraction peak of graphite oxide in the pattern of RGO, indicating that the GO was well reduced by hydrazine hydrate. [7] Also, the diffraction peaks at about 25° and 43° are attributed to (002) and (100) planes of graphite-like structure.[20] In the pattern of CeO_2–RGO, we can see that the major diffracted peaks are the same as those of as-synthesized CeO_2 nanoparticles demonstrating that CeO_2 nanoparticles were successfully anchored on the RGO sheets. These patterns show the typical cubic fluorite-type structure of CeO_2 (JCPDS no. 34-0394) suggesting the successful formation of the CeO_2 phase.

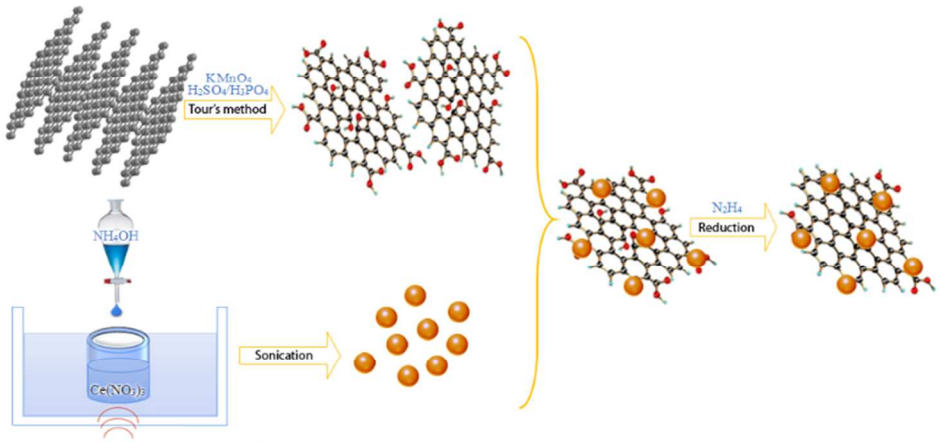

Scheme 1. Schematic illustration for the synthesis of the CeO_2–RGO nanocomposite.

Journal Name

RSCPublishing

ARTICLE

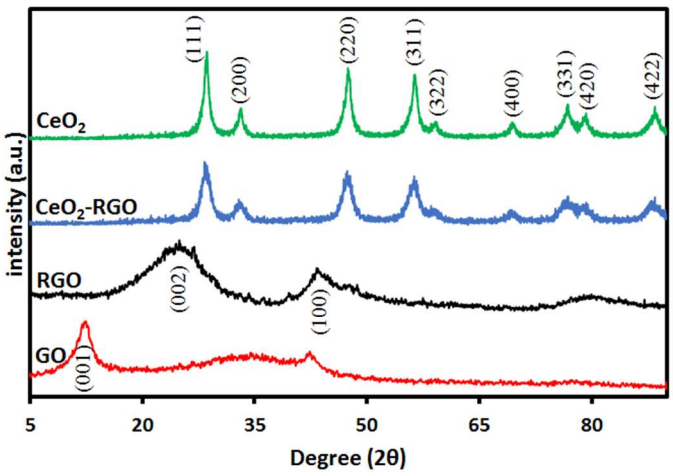

Fig. 1. X-ray diffraction patterns of GO, RGO, CeO_2 and CeO_2–RGO nanocomposite.

FE-SEM & EDX. The FE-SEM image of the CeO2–RGO nanocomposite (Fig. 2c) confirms the good combination of RGO and CeO2 nanoparticles. The particle size distribution of anchored CeO2 nanoparticles on RGO is similar to the CeO2 nanoparticles with a grain size in the range of 20–30 nm (Fig. 2b). Also, Fig. 2a reveals that the RGO is composed of wrinkled and layered thin platelet sheets. Furthermore, the energy-dispersive X-ray (EDX) analyses were obtained for as prepared materials to confirm the existence of Cerium, Oxygen and Carbon as the elementary components in the nanocomposite (Fig. 3).

FT-IR study. The FT-IR spectra of GO, RGO, CeO_2 and CeO_2–RGO nanocomposite are shown in Fig. 4. The FT-IR spectrum of GO exhibits absorption bands at 1735 cm^{-1} and 1050 cm^{-1}, attributing to the C=O and C-OH stretching vibrations of the COOH group, respectively. The band at 1621 cm^{-1} is assigned to the bending vibration of absorbed water molecules and the contributions of the sp^2 characteristics, whereas, for the epoxy groups, a band at 1225 cm^{-1} can also be seen.

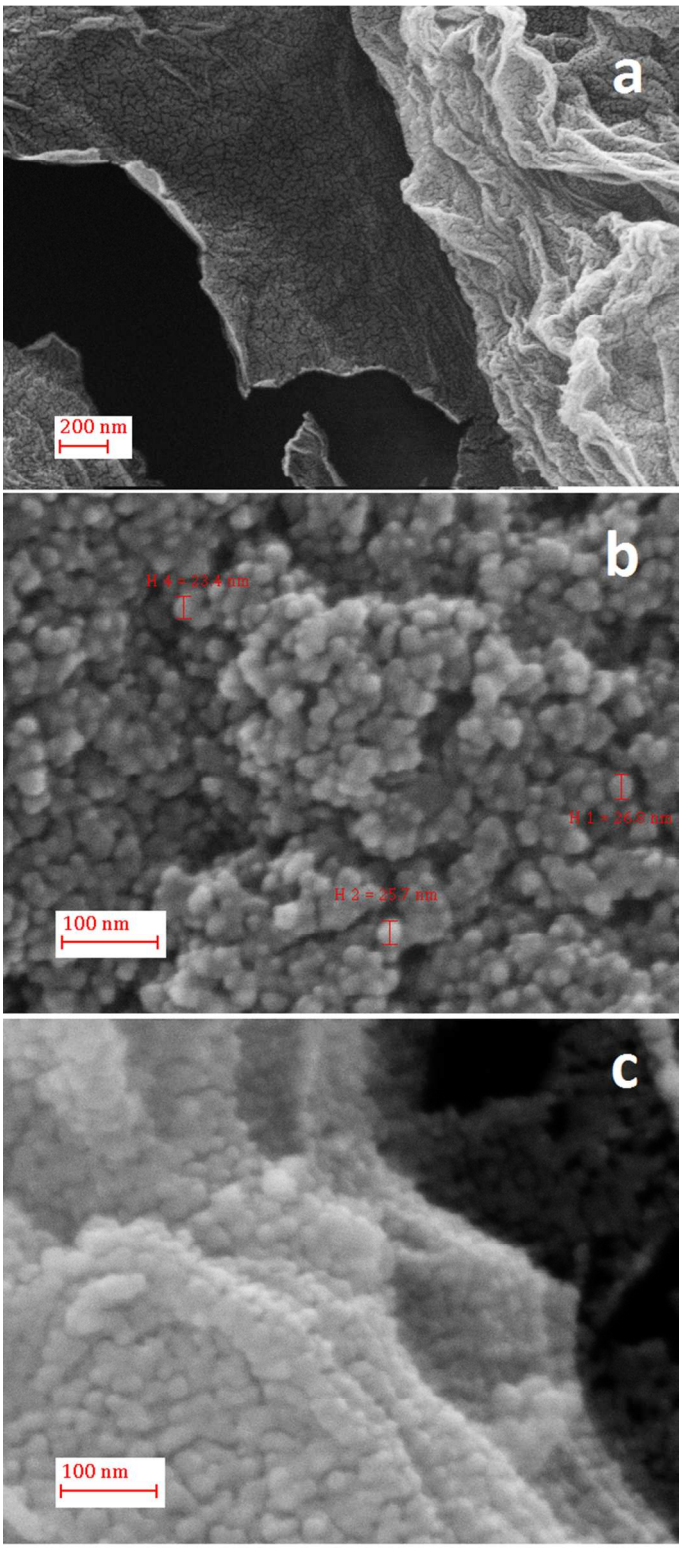

Fig. 2. FE-SEM image of a) RGO, b) CeO_2 and c) CeO_2-RGO.

The bands at 3398 cm^{-1} and 1397 cm^{-1} are attributed to the –OH stretching and deformation vibrations, respectively. In the FT-IR spectra of RGO and CeO_2–RGO, the absorption band at 1735 cm^{-1} is disappeared indicating the removal of the oxygen-containing functional groups. The FT-IR spectrum of CeO_2 shows a band at 505 cm^{-1} attributed to the Ce–O vibration of the CeO_2 crystal. Also, the band at 1622 cm^{-1} is related to the bending mode of the hydroxyl groups. The bands at 1624 cm^{-1} and 1578 cm^{-1} in the FT-IR spectrum of the CeO_2–RGO nanocomposite represent the characteristic bands of graphene. Moreover, the interaction between CeO_2 nanoparticles and RGO is illustrated by the band at 489 cm^{-1}.[17, 21]

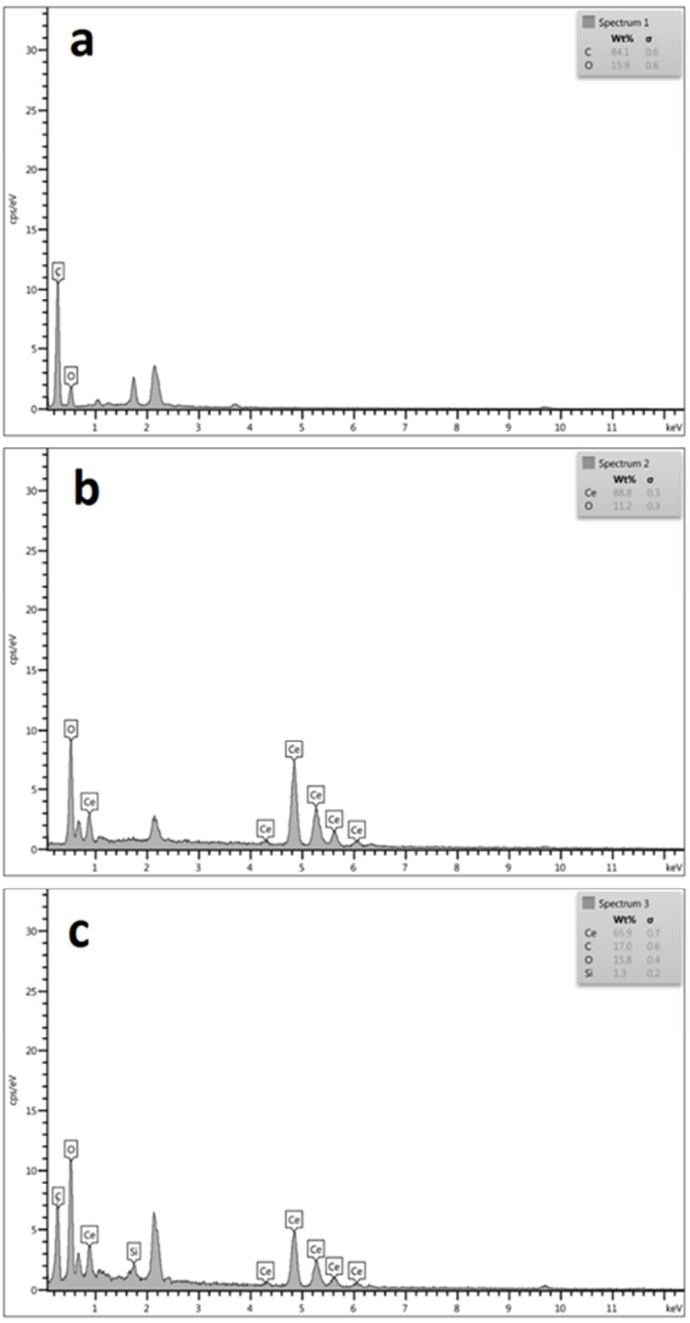

Fig. 3. EDX analyses of a) RGO, b) CeO_2, c) CeO_2-RGO.

Raman spectroscopy. Fig. 5 shows the Raman spectra of GO, RGO, CeO_2 and CeO_2–RGO nanocomposite. Two main peaks at 1360 cm-1 and 1599 cm-1 can be seen in the Raman spectrum of GO which correspond to the D and G bands, respectively.

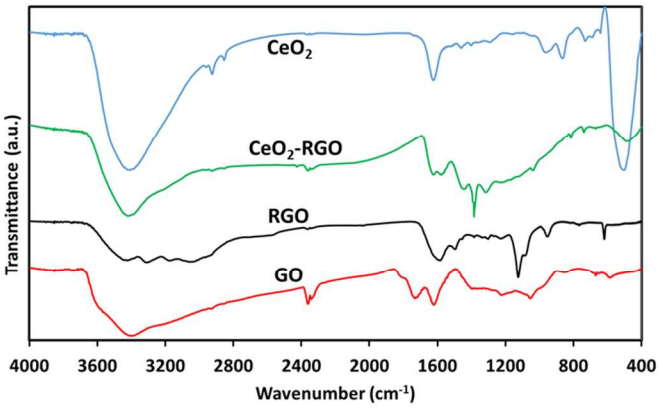

Fig. 4. FT-IR spectra of GO, RGO, CeO_2 and the CeO_2–RGO nanocomposite.

These characteristic peaks are similar for RGO and CeO_2–RGO; the D band at 1348 cm^{-1}, and the G band at 1600 cm^{-1}. The D band is associated with the structural defects such as bond length disorder, bond-angle disorder, and hybridization which can break the symmetry and selection rules, whilst the G band is related to the in-plane vibration of C sp^2 atoms.[6, 10, 21, 22] In the Raman spectrum of CeO_2, the intense peak at 463 cm^{-1} is attributed to the symmetrical stretching mode of the Ce–O_8 vibrational unit.[21, 22] The presence of this peak in the CeO_2–RGO nanocomposite, with a blue shift to 459 cm^{-1}, shows that the CeO_2 nanoparticles are successfully anchored on RGO. This blue shift is pertained to the charge transfer between CeO_2 and RGO.[6, 21, 22]

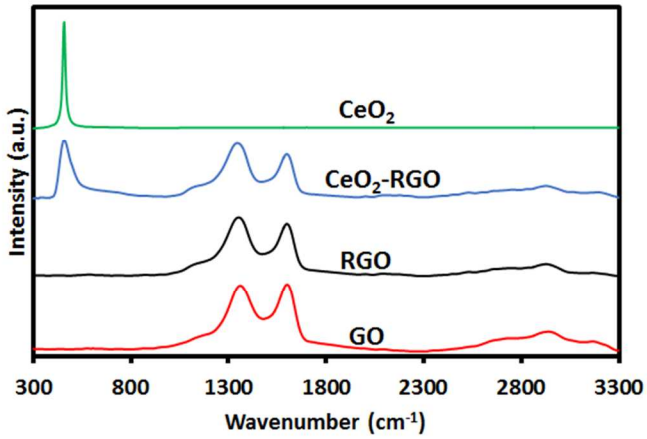

Fig. 5. Raman spectra of GO, RGO, CeO_2 and CeO_2–RGO nanocomposites.

The investigation of the intensity ratios of D to G (I_D/I_G) bands allow us to estimate the size of the in-plane crystallites (L_a) in the unit of nm by using the Tunistra-Koening relation.[6, 23]

$$L_a = (2.4\times10^{-10})\lambda^4(I_D/I_G)^{-1}$$

Where λ is the laser excitation wavelength (532 nm in this study).

The ratio of I_D/I_G (~ 1.25) is almost the same for the RGO and CeO_2–RGO nanocomposite with the size of sp^2 graphitic area of ~15.4 nm. This illustrates that the anchoring of CeO_2 onto RGO has no effect on the crystalline sp^2 area. The Raman spectrum of the GO exhibits a I_D/I_G ratio of ~0.98 with the in-plane crystallite size of ~19.6 nm suggesting that the defects are less present in comparison to RGO.

Electrochemical studies

CV. To test the supercapacitive performance of pure CeO_2, RGO and CeO_2-RGO nanocomposite electrodes, CV was firstly recorded in a three-electrode system using Ag/AgCl as the reference and platinum foil as the counter-electrode. The capacitive behavior of pure CeO_2, RGO and CeO_2-RGO nanocomposite electrodes was systematically examined in this work and typical CV curves of pure CeO_2, RGO and CeO_2-RGO measured at 30 mV s^{-1} in 0.5 M Na_2SO_4 which are shown in Fig. 6a. The CV curves of CeO_2-RGO show approximate mirror images with respect to the zero-current line and a rapid current response to voltage reversal at each end potential (the quasi-rectangular shapes and symmetric I–V responses) indicating the ideal pseudocapacitive behavior of the materials. For the CeO_2 electrode active material, the oxidation and reduction reactions could be as follows:

$$CeO_2 + M^+ + e^- \leftrightarrow CeOOM$$

Where M represents hydrated protons (H_3O^+) and/or alkali cations such as K^+, Na^+, and Li^+. According to the CV curve of CeO_2-RGO, one reversible electron-transfer process is observed, which is consistent with the reaction process mentioned above during the potential sweep of CeO_2-RGO electrode, demonstrating that the capacitance of CeO_2-RGO is on the basis of the redox mechanism: during the charging process the electrode reaction corresponds to the oxidation of CeO_2 to CeOOM, while during the discharging process, the electrode reaction corresponds to the reduction of CeOOM to CeO_2. The CV curve of pure CeO_2, RGO electrode measured under the same conditions shows that the current is smaller than that of the CeO_2-RGO electrode. In the CeO_2-RGO nanocomposite, the synergistic effect is found by combining CeO_2 and RGO, reasonably resulted from the uniform dispersion of CeO_2 nanocrystals onto the surface of RGO sheets and better electronic conductivity of the RGO. Hence, a high electrochemical performance can be achieved and the specific capacitance values of CeO_2, RGO and CeO_2-RGO are equal to 91, 86 and 211 F g^{-1} at scan rate 2 mV s^{-1}, respectively (only deposited weight of CeO_2, RGO and CeO_2-RGO material is considered in calculations). The specific capacitance of supercapacitors can be estimated by the following equation[24]:

$$SC = \frac{1}{v(V_c - V_a)} \int_{V_a}^{V_c} I \, dV$$

Where *SC* is the specific capacitance (F g^{-1}), *v* is the potential scan rate (mV s^{-1}), V_c - V_a is the potential range and *I* denotes the response current (mA g^{-1}) based on the mass of electroactive material. Fig. 6b and 6c show the CV curves of

the RGO and CeO_2-RGO electrodes at different scan rates of 10, 20, 40, 60 and 75 mV s^{-1} in a potential range of -0.8 to 0.6 V. No curve shows significant changes in the rectangular shape with increasing scan rate, indicating highly reversible redox reactions. This shows stability of electrolytes in the supercapacitor. The reduction of specific capacitance as a function of the sweep rates for the CeO_2-RGO electrode are calculated in Fig. 6d. In this plot specific capacitances for CeO_2-RGO electrode decreased from 211 to 113 F g^{-1} with the increase of the potential sweep rate from 2 to 200 mV s^{-1}. Based on these results, it could be suggested that at low scan rates, the electrolyte ion (Na^+ or H^+) can be inserted into the available pores in the CeO_2-RGO structure, which lead to a higher effective the redox reaction and a high capacitance. But as the scan rate is increased to 200 mV s^{-1}, the effective interaction between electrolyte ion and pores is significantly reduced. The effective redox reaction occurred only to the outer surface of the supercapacitor electrode, which caused a decline in the total capacitance.[25]

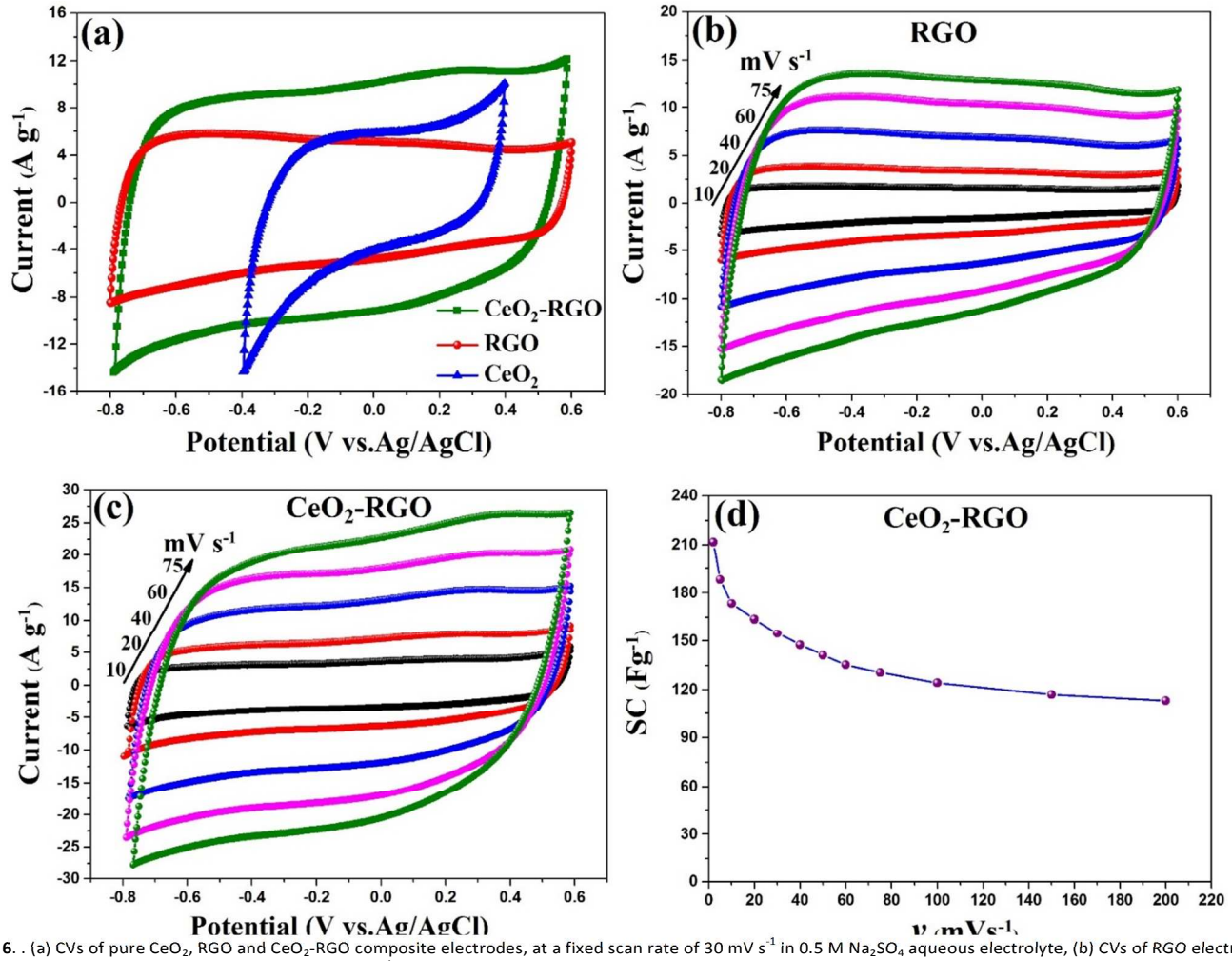

Fig. 6. . (a) CVs of pure CeO_2, RGO and CeO_2-RGO composite electrodes, at a fixed scan rate of 30 mV s^{-1} in 0.5 M Na_2SO_4 aqueous electrolyte, (b) CVs of RGO electrode at different scan rates of 10, 20, 40, 60 and 75 mV s^{-1} in a potential range of -0.8 to 0.6 V in 0.5 M Na_2SO_4 aqueous electrolyte, (c) CVs of CeO_2-RGO nanocomposite electrode at different scan rates of 10, 20, 40, 60 and 75 mV s^{-1} in a potential range of -0.8 to 0.6 V in 0.5 M Na_2SO_4 aqueous electrolyte and (d) Specific capacitance as a function of sweep rate for CeO_2-RGO nanocomposite electrode, specific capacitance decreased from 211 to 113 F g^{-1} with increase of potential sweep rate from 2 to 200 mV s^{-1}.

CCV. CCV technique could be considered the best tool for examination of the monitoring in the CVs and charge storage of a capacitor during the time.[15, 16] The long-term cycle stability of RGO and CeO_2-RGO nanocomposite electrodes is evaluated by repeating the CCV technique at a scan rate 250 mV s^{-1} for 4000 cycles. The specific capacitance as a function of time is presented in Fig. 7a. It can be seen that the capacitance of the CeO_2-RGO nanocomposite electrode increases slightly at the beginning and then remains almost constant. Finally, the specific capacitance almost keeps stability until 4000 cycles (5.6 % increase). Also, the RGO electrode after 4000 cycles, the specific capacitance is increased only about 0.9%. The above results demonstrate that CeO_2-RGO nanocomposite electrode is highly stable during a cycling test and also in comparison to RGO electrode, shows a much higher cycle stability and much higher specific capacitance as shown in Fig. 7a. . Fig. 7b and 7c present three-dimensional (3D) CCVs which were performed during 45000 seconds at a scan rate of

250 mV s^{-1}. In these two 3D-plots, the CV changes over time are visible as well.

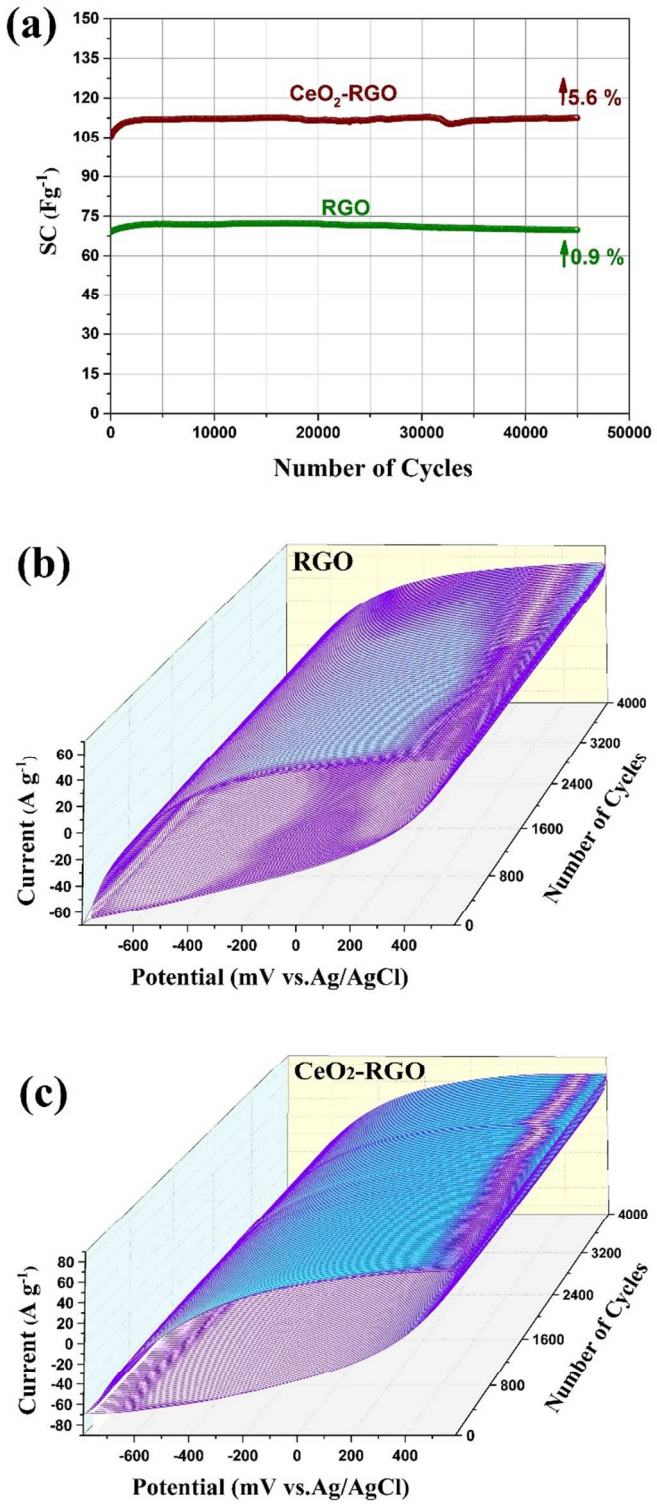

Fig. 7. Variation of the specific capacitance of the RGO and CeO_2-RGO nanocomposite electrodes as a function of time measured at 250 mV s^{-1} and 3D-CCV curves of RGO and CeO_2-RGO composites electrodes measured at scan 250 mV s^{-1} (b, c).

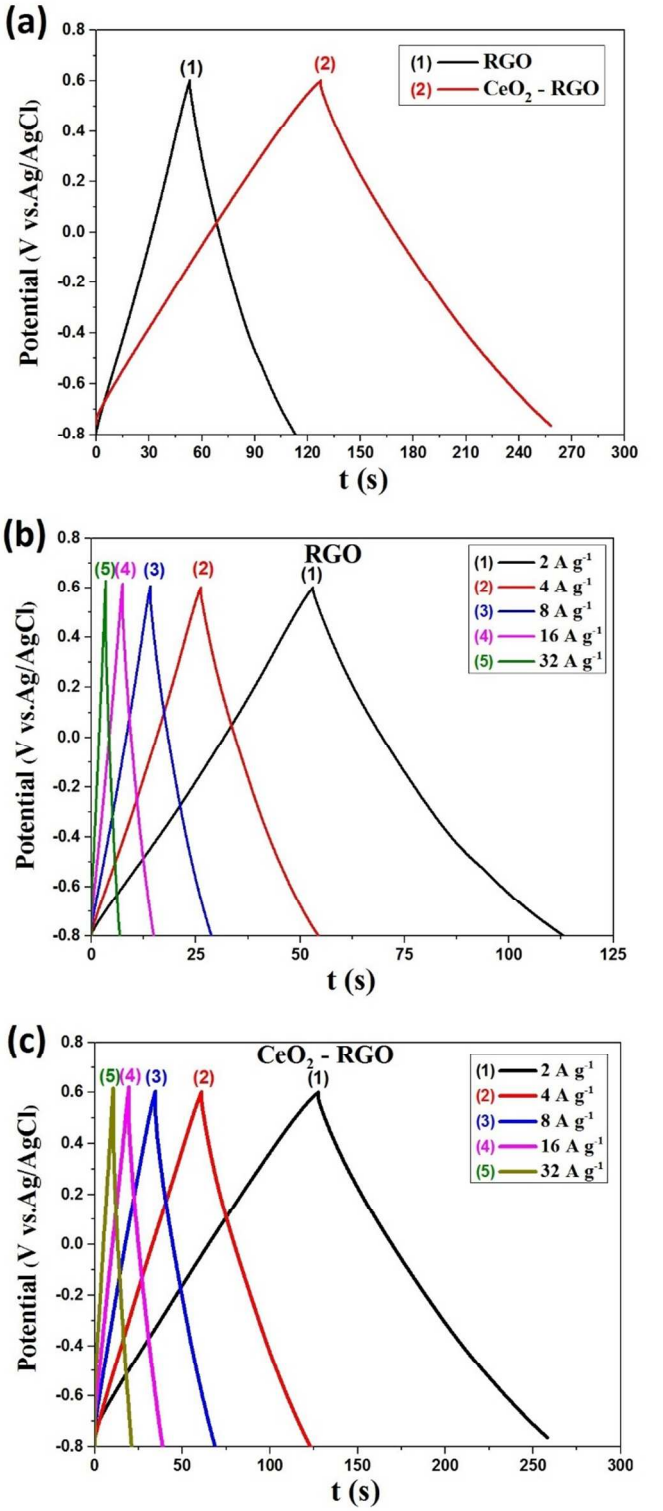

Fig. 8. Chronopotentiograms of RGO and CeO_2-RGO at charge–discharge current density of 2.0 A g^{-1} (a) and Chronopotentiograms of the RGO and CeO_2-RGO composite electrode at different charge–discharge current densities between -0.8 and 0.6 V (b, c)

Charge/Discharge. Another electrochemical test used to evaluate the supercapacitive performance of the samples is chronopotentiometry. Fig. 8a exhibits the chronopotentiogram

curves of RGO and CeO_2-RGO nanocomposite electrodes with various ratios at a current density of 2.0 Ag^{-1}. All chronopotentiograms exhibit an equilateral triangle shape, suggesting a good reversibility and ideal capacitive behavior during the charge/discharge processes. The good capacitive behaviors of electrode materials would be attributed to the following features: (1) the RGO with a good electrical conductivity and reduced internal resistance of CeO_2 nanoparticles; (2) Uniform distribution of CeO_2 nanoparticles on the surface of RGO facilitated the charge transport from CeO_2, leading to rapid redox reactions. The SC values were calculated from charge/discharge cycles using the following equation:[3]

$$SC = \frac{It_d}{mV}$$

Where I is the charge/discharge current (A), t_d is the discharge time (s), m is the active mass (g) and V is the potential drop during discharge (V). The SC values of RGO and CeO_2-RGO nanocomposite electrodes are 85 and 185 F g^{-1} at the current density of 2 A g^{-1}. Fig. 8b and 8c show the chronopotentiogram curves of RGO and CeO_2-RGO nanocomposite electrodes in the potential region of -0.8 to 0.6 V at different current densities, ranging from 2 to 32 A g^{-1}. The curves are linear, triangular-shaped, very sharp and symmetric. Also the durations of charging and discharging are almost equal for each electrode, implying a high columbic efficiency, reversible behavior, and ideal capacitor performance.

EIS. The EIS analysis is an important technique for investigation of the supercapacitive performance and typical resistance of electrode materials for supercapacitors. The Nyquist impedance plots (imaginary part, Z', versus real part, Z") for CeO_2, RGO and CeO_2-RGO nanocomposite electrodes at an applied potential of 0.0 V (about the midpoint of the cyclic voltammetry range) in 0.5 M Na_2SO_4 solutions over the frequency range 0.01–10^5 Hz is shown in Fig. 9. The plots are composed of a small semicircle at high frequency region and of a line in the lower frequency region. The large semicircle observed for the electrode is indicative of high interfacial charge-transfer resistance (R_{ct}), relating to the poor electrical conductivity of materials, whereas the more vertical line related to an electrode more close to an ideal capacitor.[26, 27]

The impedances at high frequency reflect the equivalent series resistance (ESR) in the electrode/electrolyte system, which is contributed from both the electrolyte resistance and electronic resistance of textile electrodes. The equivalent ESR of CeO_2, RGO and CeO_2-RGO nanocomposite electrodes obtained from the intersection of the Nyquist plot at the x-axis is 0.43 Ω, 0.36 Ω, and 0.36 Ω, respectively.

These ESR values of the electrodes, reveal the small changes in conductivities and morphologies of electrode surface by changing the material composition.[27] In fact, the addition of RGO reduces the value of ESR because of its good electrical conductivity or enhancing the electrode surface.

However, as shown in the figure, a significant change in R_{ct} occurs by adding CeO_2-RGO to the electrode material. According to the diameter of the semicircle, the R_{ct} of CeO_2, RGO and CeO_2-RGO nanocomposite electrodes are 15.4 Ω, 10.4 Ω, and 7.5 Ω, respectively. The low electrical conductivity of CeO_2 results in the significant R_{ct} for CeO_2. In contrast, RGO shows a smaller R_{ct} due to its good conductivity. The value of R_{ct} of CeO_2-RGO could be a good evidence of catalytic effect of CeO_2, or the synergistic effect of combination of CeO_2 and RGO.[2, 7, 21, 28] In other words, the substantial reduction in the R_{ct} of electrodes could be related to the enhancement in the rate of charge transfer of the ions at CeO_2-RGO materials.

Meanwhile, the straight line of the Nyquist plot at high frequency is related to the Warburg resistance resulting from the frequency dependence of ion diffusion/transport in the electrolyte.[27, 29] The large Warburg region of these electrodes shows the greater variations in ion diffusion path lengths and increased obstruction of ion movement. Therefore, the high resistance of ion transfer in RGO electrode, significantly the capacitance of the electrode is reduced. In contrast, CeO_2-RGO exhibited a short diffusion path length of ions in the electrolyte, which could be seen from the low resistance of the capacitive part on the Nyquist plot. Indeed, a synergistic effect in CeO_2 and RGO leading to a lower resistance of ion transfer. Moreover, the presence of RGO with high electrical conductivity resulted in a lower resistance of charge transfer.

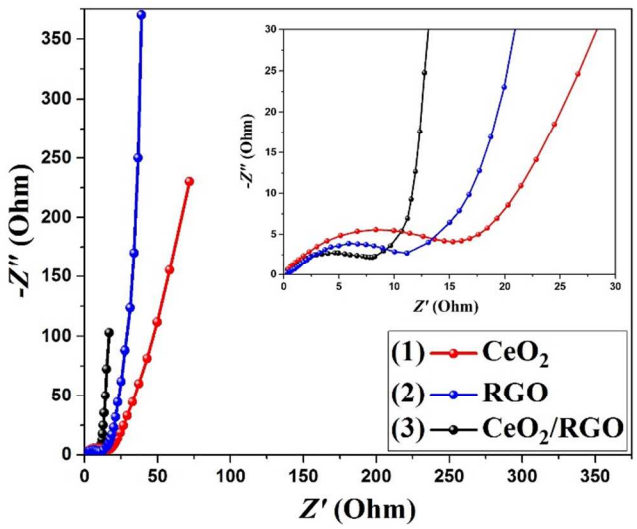

Fig. 9. Impedance spectra of supercapacitor cell having CeO_2, RGO and CeO_2-RGO nanocomposite electrodes, measured at an AC amplitude of 5 mV, in 05 M Na_2SO_4 aqueous electrolyte.

Conclusion

In summary, CeO_2 nanoparticles grown on RGO sheets have been fabricated by a facile sonochemical Method. FE-SEM images showed that CeO_2 nanoparticle uniformly covered RGO surface. Electrochemical investigation indicated that the CeO_2-RGO nanocomposite electrode had a maximum capacitance of 211 F g^{-1} and possessed regular capacitive behaviours and good cycling stabilities. The cycle stability of CeO_2 nanoparticles is

obviously enhanced by adding RGO sheets. The CCV results show the excellent long cycle life of the composite electrodes (5.2 % increased after 5000 cycles). Moreover, the composite of CeO_2 nanoparticles and RGO sheets show excellent electrochemical properties for energy storage applications, which evidence their potential for application as supercapacitors.

Acknowledgements

The authors would like to thank the University of Tehran (6102027) for financial support of this work as grants. The authors would like to thank Amir Mahyar Azhdarpour for taking FE-SEM images.

Notes and references

[a] Center of Excellence in Electrochemistry, Faculty of Chemistry, University of Tehran, Tehran, Iran.
[b] Biosensor Research Center, Endocrinology & Metabolism Molecular-Cellular Sciences Institute, Tehran University of Medical Sciences, Tehran, Iran.

1. Z.-S. Wu, G. Zhou, L.-C. Yin, W. Ren, F. Li and H.-M. Cheng, *Nano Energy*, 2012, **1**, 107-131.
2. Y. Wang, C. X. Guo, J. Liu, T. Chen, H. Yang and C. M. Li, *Dalton transactions*, 2011, **40**, 6388-6391.
3. H. R. Naderi, H. R. Mortaheb and A. Zolfaghari, *Journal of Electroanalytical Chemistry*, 2014, **719**, 98-105.
4. A. G. Pandolfo and A. F. Hollenkamp, *Journal of Power Sources*, 2006, **157**, 11-27.
5. A. Ambrosi, A. Bonanni, Z. k. Sofer, J. S. Cross and M. Pumera, *Chemistry-a European Journal*, 2011, **17**, 10763 –10770.
6. D. Joung, V. Singh, S. Park, A. Schulte, S. Seal and S. I. Khondaker, *Journal of Physical Chemistry C*, 2011, **115**, 24494-24500.
7. L. H. Jiang, M. G. Yao, B. Liu, Q. J. Li, R. Liu, H. Lv, S. C. Lu, C. Gong, B. Zou, T. Cui, B. B. Liu, G. Z. Hu and T. Wagberg, *Journal of Physical Chemistry C*, 2012, **116**, 11741-11745.
8. S. P. Yu, Q. B. Liu, W. S. Yang, K. F. Han, Z. M. Wang and H. Zhu, *Electrochimica Acta*, 2013, **94**, 245-251.
9. H. Teymourian, A. Salimi and S. Khezrian, *Biosens Bioelectron*, 2013, **49**, 1-8.
10. Z. Y. Ji, X. P. Shen, M. Z. Li, H. Zhou, G. X. Zhu and K. M. Chen, *Nanotechnology*, 2013, **24**.
11. R. B. Rakhi, W. Chen, D. Cha and H. N. Alshareef, *Journal of Materials Chemistry*, 2011, **21**, 16197.
12. W. He, J. Lin, B. Wang, S. Tuo, S. T. Pantelides and J. H. Dickerson, *Phys Chem Chem Phys*, 2012.
13. B. Wang, J. Park, C. Wang, H. Ahn and G. Wang, *Electrochimica Acta*, 2010, **55**, 6812-6817.
14. D. C. Marcano, D. V. Kosynkin, J. M. Berlin, A. Sinitskii, Z. Z. Sun, A. Slesarev, L. B. Alemany, W. Lu and J. M. Tour, *ACS nano*, 2010, **4**, 4806-4814.
15. P. Norouzi, B. Larijani, M. Ezoddin and M. R. Ganjali, *Materials Science and Engineering: C*, 2008, **28**, 87-93.
16. P. Norouzi, T. M. Garakani and M. R. Ganjali, *Electrochimica Acta*, 2012, **77**, 97-103.
17. S. Zhu, J. Guo, J. Dong, Z. Cui, T. Lu, C. Zhu, D. Zhang and J. Ma, *Ultrasonics sonochemistry*, 2013, **20**, 872-880.
18. J. H. Bang and K. S. Suslick, *Advanced Materials*, 2010, **22**, 1039-1059.
19. P. Pankaj, *Theoretical and experimental sonochemistry involving inorganic systems*, Springer, New York, 2010.
20. Q. Ling, M. Yang, R. C. Rao, H. X. Yang, Q. Y. Zhang, H. D. Liu and A. M. Zhang, *Applied Surface Science*, 2013, **274**, 131-137.
21. M. Srivastava, A. K. Das, P. Khanra, M. E. Uddin, N. H. Kim and J. H. Lee, *Journal of Materials Chemistry A*, 2013, **1**, 9792-9801.
22. L. H. Jiang, M. G. Yao, B. Liu, Q. J. Li, R. Liu, Z. Yao, S. C. Lu, W. Cui, X. Hua, B. Zou, T. Cui and B. B. Liu, *Crystengcomm*, 2013, **15**, 3739-3743.
23. F. Tuinstra, *The Journal of Chemical Physics*, 1970, **53**, 1126.
24. X. Xie and L. Gao, *Carbon*, 2007, **45**, 2365-2373.
25. S. Ardizzone, G. Fregonara and S. Trasatti, *Electrochimica Acta*, 1990, **35**, 263-267.
26. A. Zolfaghari, H. R. Naderi and H. R. Mortaheb, *Journal of Electroanalytical Chemistry*, 2013, **697**, 60-67.
27. J. Zhang, J. Jiang and X. S. Zhao, *The Journal of Physical Chemistry C*, 2011, **115**, 6448-6454.
28. Z. Gao, J. Wang, Z. Li, W. Yang, B. Wang, M. Hou, Y. He, Q. Liu, T. Mann, P. Yang, M. Zhang and L. Liu, *Chemistry of Materials*, 2011, **23**, 3509-3516.
29. M. Pasta, F. La Mantia, L. Hu, H. D. Deshazer and Y. Cui, *Nano Research*, 2010, **3**, 452-458.

